

# Quasi-Geostrophic Controls on Precipitating Ascent in Monsoon Depressions

VARUN S. MURTHY\*

*Department of Geology and Geophysics, Yale University, New Haven, Connecticut*

WILLIAM R. BOOS

*Department of Earth and Planetary Science, University of California, Berkeley, and  
Climate and Ecosystem Sciences Division, Lawrence Berkeley National Laboratory, Berkeley, California*

## ABSTRACT

South Asian monsoon depressions are convectively coupled cyclonic vortices that form and intensify in a region of easterly vertical shear of the horizontal wind. Observations of maximum precipitation down-shear of the cyclonic center have led to prior theories of quasi-geostrophic (QG) control of moist convection in these storms, and this study examines the interaction between adiabatic QG lifting and moist convection in monsoon depressions using an atmospheric reanalysis and idealized model. Inversion of the QG omega equation in the reanalysis shows that, in the down-shear, heavily precipitating region, adiabatic QG ascent, due to advection of vorticity and temperature, is comparable to diabatic ascent in the lower troposphere, while diabatic ascent dominates in the middle and upper troposphere. The causal influence of adiabatic QG lifting on precipitating ascent in monsoon depressions is then examined in the Column-QG modeling framework, where moist convection evolves in the presence of vorticity and temperature advection. The heavy observed precipitation rates are only simulated when moist convective heating amplifies QG ascent, with this interaction accounting for roughly 40% of the increase in precipitation relative to the basic state. Another 40% of this increase is produced by enhanced surface wind speed in the surface enthalpy flux parameterization, which represents the effect of cyclonic winds in the monsoon depression. Horizontal advection of the mean-state poleward moisture gradient accounts for the remaining 20% of the precipitation increase. In the up-shear region, adiabatic QG subsidence and horizontal moisture advection both suppress precipitation, and are opposed by wind-enhanced surface enthalpy fluxes.

## 1. Introduction

Monsoon depressions (MDs) are synoptic-scale, cyclonic vortices that are a key component of the South Asian monsoon (Ramage 1971). Most MDs form over the Bay of Bengal and propagate northwest over India, collectively producing a large fraction of the total monsoon precipitation (Sikka 1977; Yoon and Chen 2005). While some structural similarities exist between MDs and early-stage tropical cyclones (i.e., tropical depressions), MDs typically do not attain typhoon intensities due to the strong vertical wind shear of the monsoon environment. Although MDs have been studied for decades, many aspects of their intensification remain incompletely understood.

The basic state in which MDs form has strong easterly vertical wind shear, as mentioned above, in addition to strong horizontal wind shear associated with the low-level monsoon westerlies. This background state has motivated several prior theories for MD intensification. Some

early theories invoked baroclinic instability (e.g., Saha and Chang 1983), with cumulus heating likely being required for growth given the observed magnitude of the easterly vertical shear (Moorthi and Arakawa 1985). However, Cohen and Boos (2016) showed that MDs do not possess the up-shear vertical tilt required for baroclinic growth, seemingly ruling out that amplification mechanism. Alternatively, the strong meridional shear of the low-level monsoon westerlies motivated intensification theories based on barotropic instability (e.g., Lindzen et al. 1983). More recently, Diaz and Boos (2018) showed that barotropic instability could indeed explain some observed aspects of MDs, including their spatial scale and structure, but that interactions with moist convective heating are additionally required to produce intensification in a realistic three-dimensional (3D) basic state. Some vertical shear seems to be needed to produce that coupling with moist convection (Diaz and Boos 2019). In summary, while theories for MD intensification remain incomplete, the importance of both the basic state shear and the coupling with precipitating convection has long been recognized (e.g., Krishnamurti et al. 1976).

\*Corresponding author address: Varun S. Murthy, Department of Geology and Geophysics, Yale University, P.O. Box 208109, New Haven, CT 06520-8109.

E-mail: varun.murthy@yale.edu

Precipitating convection in MDs is localized southwest of the lower-tropospheric vorticity maximum, as expected for a balanced cyclonic vortex in easterly vertical shear (e.g., Godbole 1977; Raymond and Jiang 1990). The interaction of the synoptic-scale vortex and the background vertical shear is typically represented by the quasi-geostrophic (QG) omega equation, which provides a linear framework for examining the vertical motion response to advection of vorticity and temperature (collectively called the adiabatic forcing) and diabatic heating (see review in Davies 2015). Indeed, Sanders (1984) found that the adiabatic forcing could be prescribed in the QG omega equation to roughly diagnose the location of ascent in one MD, and Boos et al. (2015) found that it correctly diagnosed the horizontal structure of ascent in a composite of over 100 MDs. However, both of those studies and classical theory (e.g., Holton and Hakim 2013) recognize that diabatic heating can make a larger contribution than the adiabatic forcing to the amplitude of ascent obtained from the QG omega equation. For example, Shaevitz et al. (2016) found that more than half the vertical velocity diagnosed from the QG omega equation could be attributed to diabatic heating during two extreme precipitation events in the Himalayas. One goal of this study is to investigate the comparative influence of diabatic heating and adiabatic forcing on QG ascent in MDs; this is accomplished through a 3D inversion of the QG omega equation in observationally based composites.

However, diagnostic comparisons of adiabatic and diabatic QG ascent are insufficient for understanding precipitating ascent in MDs, because the moist convective heating that appears in the QG omega equation is influenced by the adiabatically forced ascent. This feedback of diabatic heating on QG ascent led Nie and Sobel (2016) to develop the Column Quasi-Geostrophic (CQG) framework in which this feedback can be explicitly represented. The CQG framework takes as input the advection of vorticity and temperature, then uses a prognostic model for moist convection to obtain the diabatic heating and thus the full QG ascent. Nie et al. (2016) used this framework to show that the positive feedback of convective heating on QG ascent was partly responsible for the intense precipitation observed during the 2010 Pakistan flood. Here we use the CQG framework to study MDs, coupling a cloud system-resolving model (CSRM) with the QG omega equation to represent precipitating vertical motion in either the ascending region southwest of the peak MD vorticity or the subsiding region to the northeast. Specifically, advection of vorticity and temperature is taken as the adiabatic forcing, and a single horizontal wavenumber is assumed to reduce the QG omega equation to one dimension. At each time step, the domain mean diabatic heating from the CSRM is used as the diabatic term in that one-dimensional (1D) QG omega equation, and vertical velocity obtained from the QG omega equation is imposed in the CSRM.

In addition to large-scale adiabatic forcing, moist convection is also influenced by tropospheric moisture (e.g., Bretherton et al. 2004), with precipitating convection in MDs occurring in regions of enhanced humidity (e.g. Hunt et al. 2016) and being suppressed during dry intrusions (Fletcher et al. 2018). Adames and Ming (2018b) argued that in synoptic-scale monsoon disturbances simulated in a general circulation model, which might include a wider set of vortices than MDs, isentropic ascent down-shear of the vortex center moistens the lower troposphere, making it conducive for deep convection. Furthermore, they argued that longwave radiative heating drove ascent in their simulated disturbances, thereby opposing dissipation of the disturbances. In another study, Adames and Ming (2018a) postulated a moisture-vortex instability mechanism for the intensification of MDs, wherein horizontal advection by cyclonic winds in a poleward moisture gradient made the region down-shear of the MD center moister and more conducive for deep convection. However, they cautioned that this mechanism produced realistic growth rates only when the meridional temperature gradient was weaker than observed while the meridional moisture gradient was strong and comparable to observations. All of this motivates our examination of the influence of horizontal moisture advection on MD precipitation using the CQG framework. Horizontal moisture advection was included as one of the forcings in the CQG formulation set forth by Nie and Sobel (2016), so we only need to estimate the magnitude of horizontal moisture advection from reanalyses and test its effect on ascent in the CQG model.

Precipitating ascent in MDs might also be influenced by wind-enhanced ocean evaporation. This process is best-known for its role in TCs, where it is termed Wind Induced Surface Heat Exchange (WISHE; Emanuel 1986) and has been the subject of much debate (e.g. Montgomery et al. 2009, 2015). Wind-enhanced surface enthalpy fluxes seem to be necessary for the sustained intensification of nascent tropical depressions in a resting basic state in idealized CSRMs (Murphy and Boos 2018). For simulations using a realistic, strongly sheared monsoon basic state, MDs can intensify even in the absence of wind-enhanced surface evaporation, but that process does increase their intensity (Diaz and Boos 2019). This motivates examination of the role of wind-enhanced surface evaporation in our CQG framework.

The next section describes the data and methods used in our observational analysis and the CQG modeling framework. Section 3 discusses results from inversion of the QG omega equation in reanalysis and section 4 presents results from the CQG model. We finish with a summary and discussion of results in section 5.

## 2. Data and Methodology

### a. Observational analysis

#### 1) ATMOSPHERIC REANALYSIS

The observational analysis in this study utilizes storm-centered composites of Indian MDs in the European Centre for Medium-Range Weather Forecasts Year of Tropical Convection (ECMWF-YOTC, henceforth YOTC) reanalysis (Moncrieff et al. 2012). This reanalysis, which includes the summer monsoon seasons of 2008 and 2009, was chosen because it provides parameterization tendencies that can be used to evaluate the diabatic term in the QG omega equation. The reanalysis uses a spectral T799 model with 97 vertical levels, and we use pressure-level data at  $1^\circ \times 1^\circ$  horizontal resolution and 6 h temporal resolution.

The YOTC reanalysis contains temperature tendencies associated with parameterizations of cloud microphysics, shallow convection, deep convection, radiation, and turbulent diffusion (Dee et al. 2011). The cloud micro-physics scheme provides temperature tendencies due to latent heating in grid-scale vertical motion, whereas the shallow and deep convection schemes estimate diabatic heating in shallow and deep convective clouds, respectively. Below 950 hPa in MDs, positive temperature tendencies from turbulent diffusion, roughly  $5 \text{ K day}^{-1}$ , cancel negative tendencies of roughly the same magnitude associated with deep convection. Therefore, we add the temperature tendencies from deep convection and turbulent diffusion and refer to the sum as ‘deep convection’.

In section 3, some storm-centered quantities are decomposed into time-mean and anomalies. Composite-mean time-means are obtained by averaging all 6-hourly states contained within the month of the storm of interest, using a storm-centered coordinate system, then averaging over all storms. Composite-mean anomalies are obtained by subtracting that storm-centered composite-mean time-mean from the storm-centered composite-mean total field.

#### 2) MONSOON DEPRESSION TRACKS

Tracks of MDs are obtained from the dataset of Hurley and Boos (2015), which identifies low pressure systems in monsoon zones by tracking 850 hPa relative vorticity maxima. We only use tracks from June–September of 2008 and 2009 that are classified as depressions or deep depressions (surface wind speeds of  $8.5 \text{ m s}^{-1}$  to  $18 \text{ m s}^{-1}$ ). Furthermore, we only include MDs that form over the Bay of Bengal and restrict ourselves to the first half of the storm life-cycle to capture characteristics typical of intensifying MDs. The resulting subset of MDs includes 7 depressions and deep depressions, with 4 in 2008 and 3 in 2009. Storm-centered composites were computed by averaging variables relative to the storm center, with 6-hourly

## Precip. anomaly and vertical shear

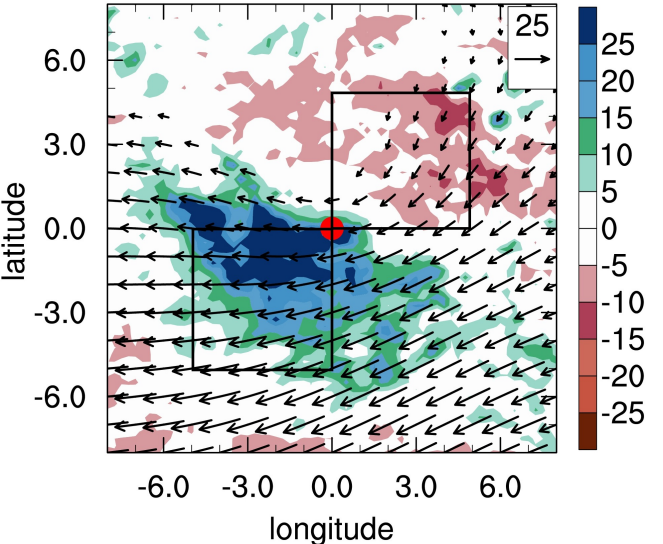


FIG. 1. Colors depict composite mean TRMM 3B42 3 hourly precipitation anomalies (units of  $\text{mm day}^{-1}$ ) at  $0.25^\circ$  horizontal resolution relative to the storm center, which is denoted by the red dot. Vectors indicate the storm-centered composite mean vertical wind shear, defined as the wind at 850 hPa subtracted from the wind at 200 hPa. The black boxes of side  $5^\circ$  depict the regions of maximum and minimum precipitation to the southwest and northeast of the MD center, respectively, and are used later to compute horizontal averages. The precipitation anomalies are computed with respect to the monthly mean TRMM 3B42 precipitation computed from 1998 to 2014.

fields first averaged for each MD and subsequently averaged over all MDs. In zonal cross-sections, we meridionally averaged across  $5^\circ$  latitude relative to the storm center. Vertical profiles were obtained by horizontally averaging in  $5^\circ \times 5^\circ$  boxes southwest and northeast of the storm center, representing the down-shear and up-shear regions, respectively (black boxes in Fig. 1).

#### 3) INVERSION OF THE QG OMEGA EQUATION

The QG omega equation (Holton and Hakim 2013) used here is

$$\left( \frac{\sigma}{f_0^2} \nabla_h^2 + \frac{\partial^2}{\partial p^2} \right) \omega = -\frac{1}{f_0} \frac{\partial}{\partial p} [-\mathbf{u}_g \cdot \nabla_h \zeta] - \frac{R}{pf_0^2} \nabla_h^2 [-\mathbf{u}_g \cdot \nabla_h T] - \frac{R}{pf_0^2} \nabla_h^2 Q, \quad (1)$$

where  $\nabla_h^2$  is the horizontal Laplacian,  $f_0$  is the planetary vorticity at the storm center,  $\mathbf{u}_g$  is the horizontal geostrophic wind computed from the YOTC geopotential,  $\sigma = -RT_0 p^{-1} d \ln \theta_0 / dp$  is the static stability,  $\zeta$  is

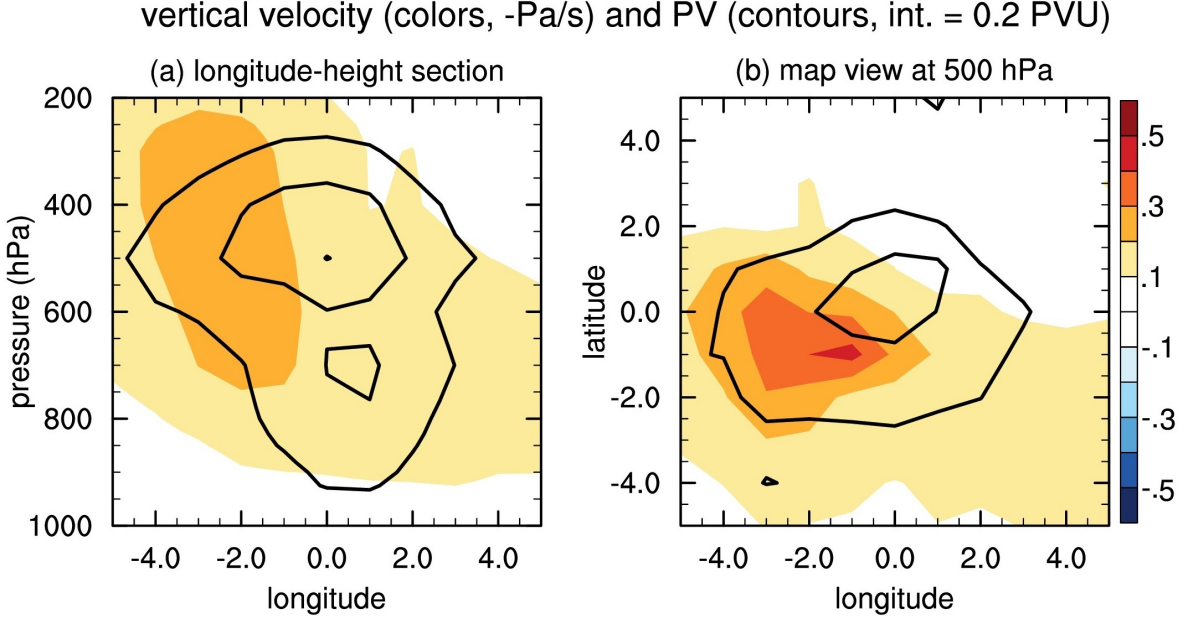


FIG. 2. Colors depict the storm-centered composite of negative vertical velocity viewed along a (a) zonal cross-section along the storm center and (b) horizontal cross-section across the storm-center at 500 hPa. Contours indicate composite mean Ertel's PV (PV) in PV units (PVU;  $1 \text{ PVU} = 10^{-6} \text{ K m}^2 \text{ kg}^{-1} \text{ s}^{-1}$ ) with contour interval of 0.2 PVU and lowest contour depicting 0.6 PVU. In (a), the variables are meridionally averaged across  $5^\circ$  latitude across the MD center.

the vertical component of the absolute vorticity of the geostrophic wind,  $T$  is the temperature,  $Q$  is the diabatic heating, and  $R$  is the gas constant for air. The first two terms on the right of Eq. (1) are the forcings due to vorticity and temperature advection, respectively, and are henceforth collectively called the adiabatic QG forcing. The third term is the diabatic QG forcing, computed here using diabatic temperature tendencies from YOTC.

Eq. (1) is inverted using the method of Shaevitz et al. (2016), and QG omega due to each of the three forcings is individually obtained. For the lower boundary condition, topographically forced vertical velocity was obtained using the geostrophic wind at the surface and the gradient of topography, following Shaevitz et al. (2016); since most of the MD tracks considered here lie over the ocean, the composite mean topographically forced vertical velocity was negligible.

### b. Idealized model

#### 1) COLUMN QG (CQG) FRAMEWORK

The CQG framework (Nie and Sobel 2016) couples parameterized large-scale dynamics with a model of convection to estimate the net vertical velocity. Briefly, the large-scale dynamics are parameterized using the 1D QG omega equation, and diabatic heating is obtained from a

3D CSRM. The 1D QG omega equation is

$$\begin{aligned} \left( -\sigma \frac{k^2}{f_0^2} + \frac{\partial^2}{\partial p^2} \right) \omega &= -\frac{1}{f_0} \frac{\partial}{\partial p} [-\mathbf{u}_g \cdot \nabla_h \zeta] \\ &\quad + \frac{Rk^2}{pf_0^2} [-\mathbf{u}_g \cdot \nabla_h T] \\ &\quad + \frac{Rk^2}{pf_0^2} Q, \end{aligned} \quad (2)$$

where  $k$  is the horizontal wavenumber,  $k = 2\pi/\lambda$ , for the wavelength  $\lambda$  characterizing the disturbance of interest. The planetary vorticity  $f_0$  is evaluated at the composite-mean storm center of  $19^\circ\text{N}$ .

After each time step of the CSRM, the CSRM domain-mean diabatic heating is used for  $Q$  and vertical profiles of horizontal advection of vorticity and temperature from the YOTC reanalysis are used for the first two terms on the right-hand side of Eq. (2). The QG vertical velocity is obtained by inverting Eq. (2) and is then used with the CSRM domain-mean vertical profiles of temperature and moisture to compute vertical advective tendencies. These tendencies are then applied to the CSRM together with tendencies of horizontal advection of temperature and moisture (obtained from YOTC), and the CSRM then takes the next time step. Here the horizontal advective tendencies of vorticity, temperature, and moisture are time invariant.

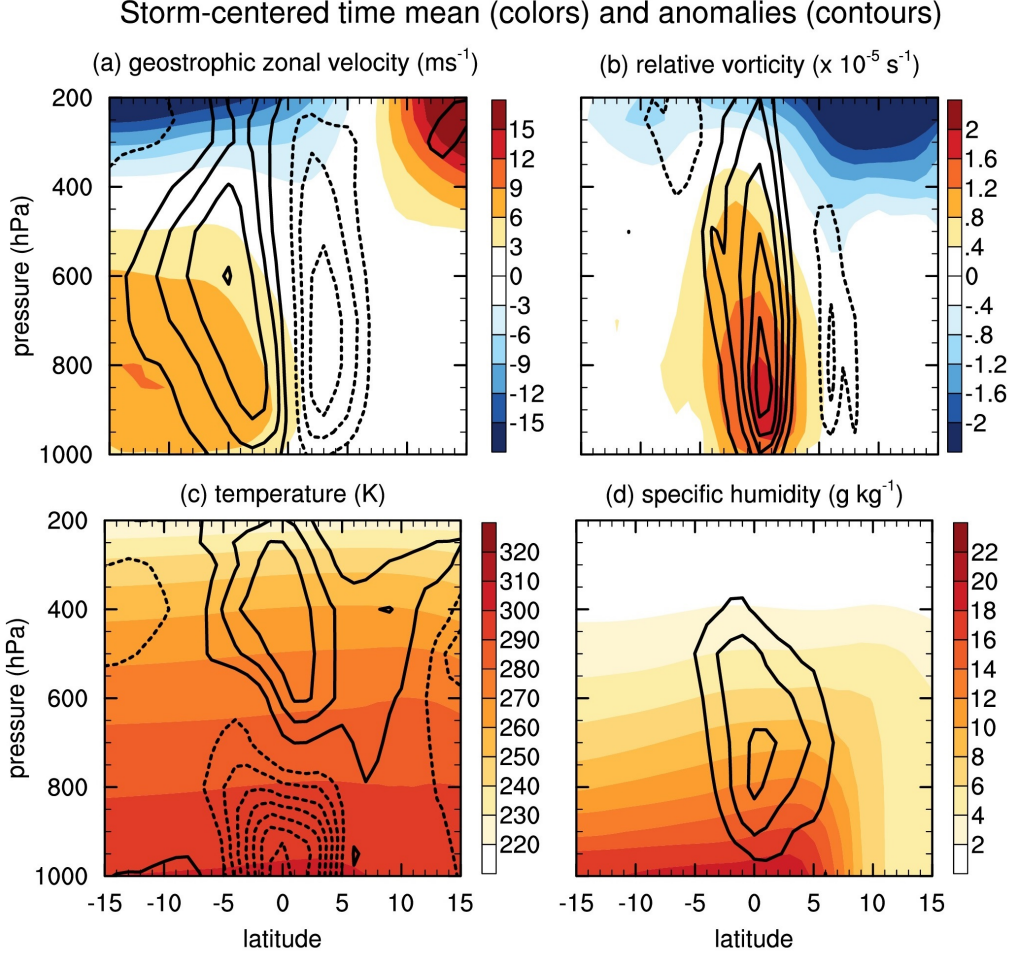


FIG. 3. Latitude-height cross sections of storm-centered time-mean (colors) and anomalies (contours, dashed negative) of (a) geostrophic zonal wind (contour interval of  $2 \text{ m s}^{-1}$ ), (b) relative vorticity (contour interval of  $10^{-5} \text{ s}^{-1}$ ), (c) temperature (contour interval of  $0.25 \text{ K}$ ), and (d) specific humidity (contour interval of  $0.5 \text{ g kg}^{-1}$ ). All quantities have been zonally averaged in a  $5^\circ$  longitude band around the storm center. Time mean quantities refer to monthly mean quantities computed from 6 hourly YOTC data from 2008 and 2009.

In reality, the evolution of the MD will result in a time-varying adiabatic forcing, but representing this would require a model for the influence of precipitating ascent on the large-scale vorticity field. This is beyond the scope of the CQG framework, and here we only examine the response to the time-invariant adiabatic forcing (and time-invariant horizontal moisture advection).

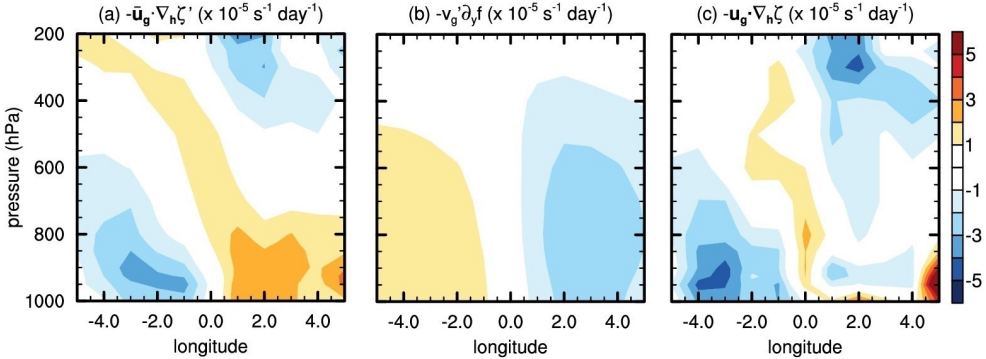
## 2) CLOUD SYSTEM-RESOLVING MODEL

The CSRM used here is version 6.8.2 of the System for Atmospheric Modeling (SAM; Khairoutdinov and Randall 2003), an anelastic, 3D, Cartesian-coordinate model whose prognostic variables are winds, liquid water/ice moist static energy, total non-precipitating water, and total precipitating water. A single moment, five species microphysics scheme represents the evolution of cloud wa-

ter, cloud ice, rain, graupel, and snow. Here, constant radiative cooling of  $1.5 \text{ K day}^{-1}$  is prescribed in the troposphere and stratospheric temperatures are relaxed to  $200 \text{ K}$  over a 5-day time scale, similar to Nie et al. (2016). A Smagorinsky-type closure is used to represent sub-grid scale turbulence. The lower boundary is an ocean with fixed sea surface temperature (SST) of  $301 \text{ K}$  and surface fluxes are computed using Monin-Obukhov similarity theory. The simulations are performed on an  $f$ -plane with Coriolis parameter  $f = 5 \times 10^{-5} \text{ s}^{-1}$ .

All simulations use a  $64 \times 64 \times 64$  grid, with horizontal resolution of  $2 \text{ km}$  and doubly periodic lateral boundaries. The lowest model level is at  $37 \text{ m}$ , and vertical resolution is roughly  $250 \text{ m}$  below  $2 \text{ km}$  and  $400 \text{ m}$  in the rest of the troposphere. The upper boundary is a rigid lid at  $27 \text{ km}$  and Newtonian damping is applied in the upper third of the domain to prevent gravity wave reflection. The model

## Advection of absolute vorticity: zonal cross-section



## Advection of absolute vorticity: map view (900 hPa)

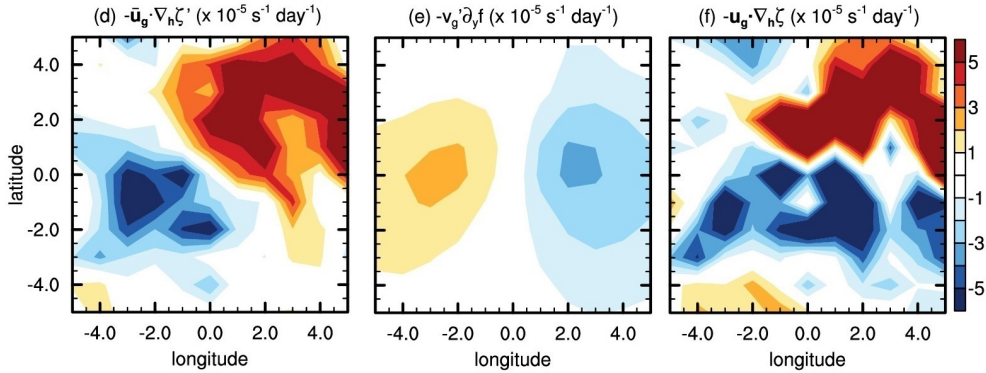


FIG. 4. Storm-centered composite mean longitude-height cross sections (upper panels) and 900 hPa map-view sections (lower panels) of the advection of absolute vorticity by horizontal geostrophic wind. The total field is depicted in the rightmost panels, with panels (a) and (b) depicting the dominant terms. Other minor terms of the decomposition are not plotted. Overbars and primes denote time-mean and anomalous quantities, respectively.

uses adaptive time stepping, with maximum time step of 5 s and automatic halving for numerical stability.

Simulations are initialized with horizontally homogeneous temperature and moisture profiles that are the horizontal average of the final 25 days of a 100 day simulation that is allowed to reach Radiative Convective Equilibrium (RCE) without QG adiabatic forcing, similar to Nie et al. (2016). The domain mean precipitation in this RCE state is roughly  $3.5 \text{ mm day}^{-1}$ . The simulations are further run for several days without QG forcing, and then up to 15 days more with QG forcing. The CSRM domain is used to represent either the region down-shear or the region up-shear of the MD center (black boxes in Fig. 1), where maximum and minimum precipitation occur, respectively. The goal is to examine the influence of QG forcing on convection in these regions, not to simulate the spinup of the MD vortex.

Since we do not simulate vortex spinup, the enhancement of surface enthalpy fluxes by the cyclonic surface winds is approximated by adding  $8 \text{ m s}^{-1}$ , which is ap-

proximately the composite mean surface wind speed in intensifying MDs in YOTC, to the wind speed at the lowest model level in the surface enthalpy flux parameterization. This surface wind enhancement is applied from the beginning of the simulation, even during the several days prior to the application of QG forcing; this allows for an assessment of the effect of wind-enhanced surface enthalpy fluxes in the absence of adiabatic QG forcing, and also may be more physically realistic since the region of QG uplift occupies only one quadrant of the region of strong cyclonic flow.

### 3. Results I: Observational composites

We begin by examining storm-centered, 3D inversions of the QG omega equation, with the goals of characterizing adiabatic and diabatic terms in that equation and creating inputs for the CQG model discussed in section 4.

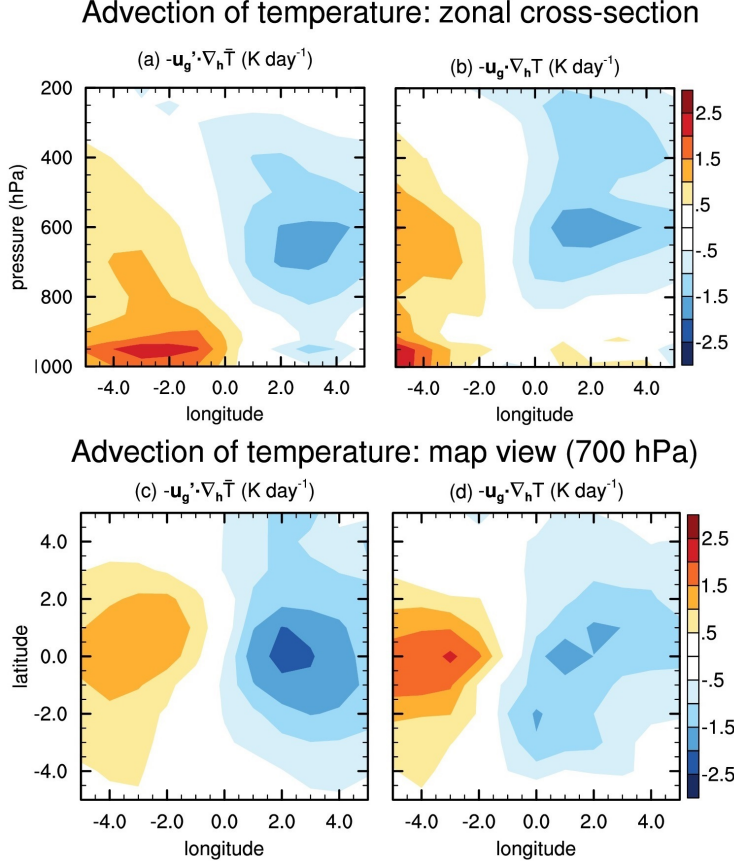


FIG. 5. Storm-centered composite mean longitude-height cross sections (upper panels) and 700 hPa map-view sections (lower panels) of the advection of temperature. The total field is depicted in the rightmost panels, with the leftmost panels depicting the dominant term. Other minor terms of the decomposition are not plotted. Overbars and primes denote time-mean and anomalous quantities, respectively.

#### a. Precipitation and ascent

First, we examine general characteristics of the set of MDs represented in the YOTC product. The composite-mean vertical wind shear, defined as the horizontal wind at 850 hPa subtracted from that at 200 hPa, is easterly at the MD center (Fig. 1, vectors). The cyclonic winds associated with the MD are relatively weak at 200 hPa compared to the background winds and do not strongly affect the vertical shear. Storm-centered composite precipitation from the Tropical Rainfall Measuring Mission (TRMM) 3B42 product shows positive anomalies down-shear (southwest) of the MD center and negative anomalies up-shear (northeast; Fig. 1), consistent with previous studies (e.g., Krishnamurti et al. 1976; Godbole 1977). These precipitation anomalies are computed relative to monthly mean TRMM precipitation, which lies between  $16 \text{ mm day}^{-1}$  and  $20 \text{ mm day}^{-1}$  in the  $10^\circ \times 10^\circ$  box surrounding the composite mean MD center. This relatively large value of monthly mean precipitation is consistent with the fact that the MD tracks are located primarily within the region of peak sea-

sonal mean rainfall over the Bay of Bengal. We delineate down-shear left and up-shear right regions (black boxes in Fig. 1), in which the horizontal mean precipitation differs by roughly  $26 \text{ mm day}^{-1}$ , that are used in subsequent sections to obtain representative vertical profiles of adiabatic QG forcing, diabatic heating, and vertical motion. The positions of these boxes could be shifted to more precisely encapsulate the wettest and driest regions, but we chose the simpler diagonal orientation shown in (Fig. 1); qualitatively similar results were obtained when these boxes were shifted to include the wettest and driest regions.

As expected, composite-mean ascent peaks at 500 hPa west and southwest of the maximum potential vorticity (PV), which tilts slightly downshear and also has peak magnitude at 500 hPa (Fig. 2). The up-shear region, northeast of the PV maximum, has weak ascent smaller than the lowest contour interval in Fig. 2. Although we expect adiabatic dynamics to force QG descent in that region, we show later that diabatic heating dominates the total vertical velocity there (furthermore, Fig. 2 shows total vertical velocity while Fig. 1 shows anomalous precipitation).

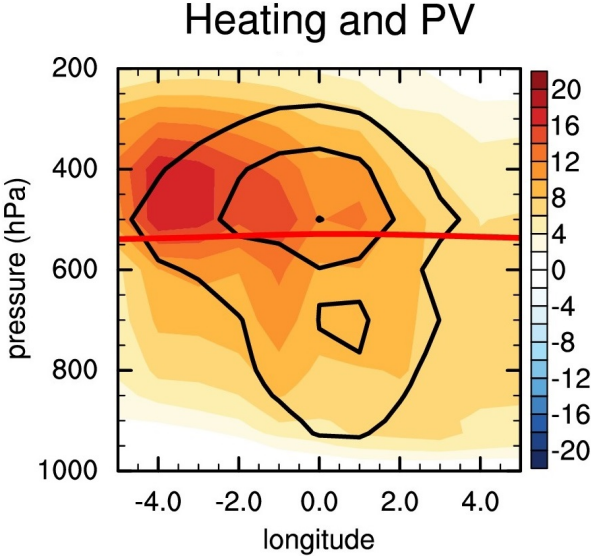


FIG. 6. Longitude-height cross sections of the storm centered composite mean diabatic heating tendency (shading, in  $\text{K day}^{-1}$ ). Contours depict PV (contour interval of  $0.2 \text{ PVU}$  and lowest contour depicting  $0.6 \text{ PVU}$ ) for reference. The red curve indicates the  $0^\circ\text{C}$  melting level.

#### b. Adiabatic advection and diabatic heating

We now examine the structure of the composite-mean MD and the background state, then show the horizontal advection of absolute vorticity and temperature, i.e., the  $-\bar{\mathbf{u}}_g \cdot \nabla_h \zeta$  and  $-\bar{\mathbf{u}}_g \cdot \nabla_h T$  components of the adiabatic QG forcing. We split quantities into time means (denoted by overbars) and anomalies (denoted by primes), representing the background monsoon state and the MD, respectively.

The storm-centered composite of the anomalous geostrophic wind depicts the cyclonic MD winds, with peak intensities between 600 hPa and 800 hPa and peak relative vorticity near 800 hPa (Fig. 3a, b, contours). The time-mean zonal wind reveals the background monsoon flow, with strong low-level westerlies south of the vortex and weak easterlies to the north (Fig. 3a, colors; low-level easterlies are weaker than the smallest colorbar level). The time-mean meridional winds in the lower troposphere are weak southerlies south of the vortex and weak northerlies to the north (not shown). The MD is centered at the poleward edge of the region of strong easterly vertical shear, in the strong background relative vorticity of the monsoon trough (Fig. 3b, colors). Thermal wind balance dictates a poleward temperature gradient of the background state and a warm-over-cold temperature anomaly in the MD (Fig. 3c). The background state also has a poleward moisture gradient, and the composite mean MD has enhanced moisture at its center (Fig. 3d).

In the composite mean, the geostrophic advection of absolute vorticity is dominated by the advection of rela-

tive vorticity of the MD by the time-mean monsoon flow,  $-\bar{\mathbf{u}}_g \cdot \nabla_h \zeta'$ , and to a smaller extent by the advection of planetary vorticity by the MD winds,  $-\nu'_g \partial_y f$  (Fig. 4). Strong low-level southwesterlies advect the vorticity of the MD to the northeast, while upper-level easterlies advect positive vorticity to the west. Advection of planetary vorticity by the anomalous cyclonic flow generally opposes this, with positive tendencies to the west and negative tendencies to the east of the MD. The total advective tendency more closely resembles  $-\bar{\mathbf{u}}_g \cdot \nabla_h \zeta'$ , with additional contributions from non-linear terms, and in the lower troposphere is negative south and southwest of the vortex center and positive to the north and northeast (Fig. 4 c,f).

The distribution of horizontal temperature advection is simpler, with advection of the background meridional temperature gradient by the anomalous cyclonic winds dominating. This produces warming, which is a QG forcing for ascent, west of the vortex, and cooling to the east (Fig. 5).

We now discuss the composite mean diabatic heating, focusing on latent heating since radiative tendencies are much weaker and more spatially homogeneous. Heating due to parameterized deep convection is the strongest constituent and is positive throughout the troposphere, with maximum values near 500 hPa down-shear of the MD center (not shown). Heating from parameterized cloud microphysics also peaks down-shear of the MD center (not shown) and has a vertical structure similar to that observed in stratiform clouds, with heating due to condensation and freezing above the melting level and cooling due to melting and evaporation below (Houze 1997). Heating by shallow convection is largely confined to the lower troposphere below 800 hPa (not shown). As a result, the total diabatic heating peaks down-shear of the MD center, with maximum values above the melting level due to superposition of tendencies from the deep-convective and microphysical schemes (Fig. 6).

#### c. Adiabatic and diabatic QG ascent

We now examine the contributions of vorticity advection, temperature advection, and diabatic heating to QG ascent obtained from a 3D inversion of the QG omega equation (with methods discussed in section 2 and by Shaevitz et al. (2016)).

The vertical gradient of vorticity advection results in QG ascent in the middle and lower troposphere and weak descent in the upper troposphere down-shear of the MD center (Fig. 7a). Up-shear of the MD center, vorticity advection results in QG ascent below 800 hPa and weak descent in the mid-troposphere. A more distinct zonal dipole of QG vertical motion results from temperature advection, with warm advection producing ascent down-shear of the MD center and cold advection producing descent up-shear (Fig. 7b).

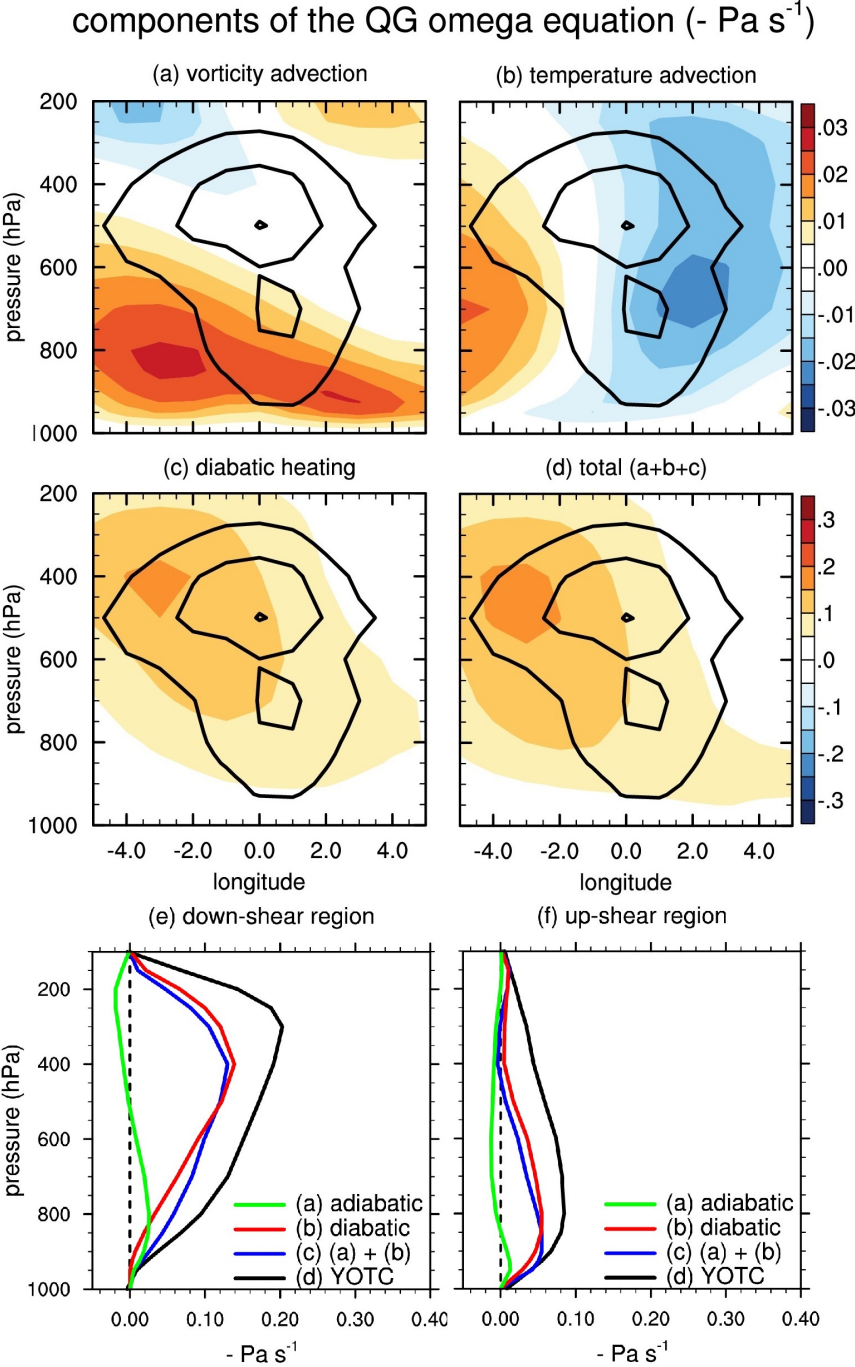
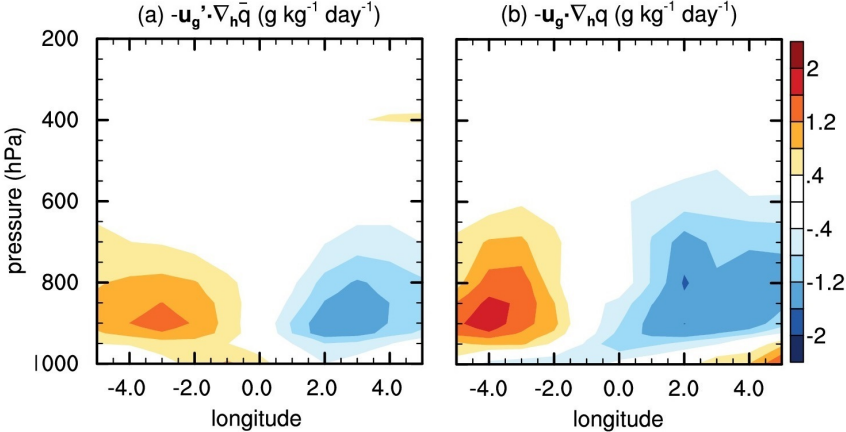


FIG. 7. Top four panels show longitude-height cross sections of the storm-centered composite mean inversion of the QG omega equation (shading, in  $\text{-Pa s}^{-1}$ ). Contours depict PV (contour interval of 0.2 PVU and lowest contour depicting 0.6 PVU) for reference. Note the change in color bar between the top two panels and the middle two panels. Lower two panels depict the vertical profiles of the storm-centered, composite mean inversion of the QG omega equation obtained by horizontally averaging quantities in the black boxes denoted in Fig. 1. Adiabatic QG vertical motion (green) includes the combined response to advection of vorticity and temperature.

Diabatic QG ascent is primarily concentrated down-shear of the MD center and is generally larger than the adiabatic components (Fig. 7c, d). Diabatic ascent has a

similar spatial structure to that of the parameterized heating, with maximum values near 400 hPa down-shear of the MD center. We also find weak diabatic ascent in the

## Advection of spec. humidity: zonal cross-section



## Advection of spec. humidity: map view (900 hPa)

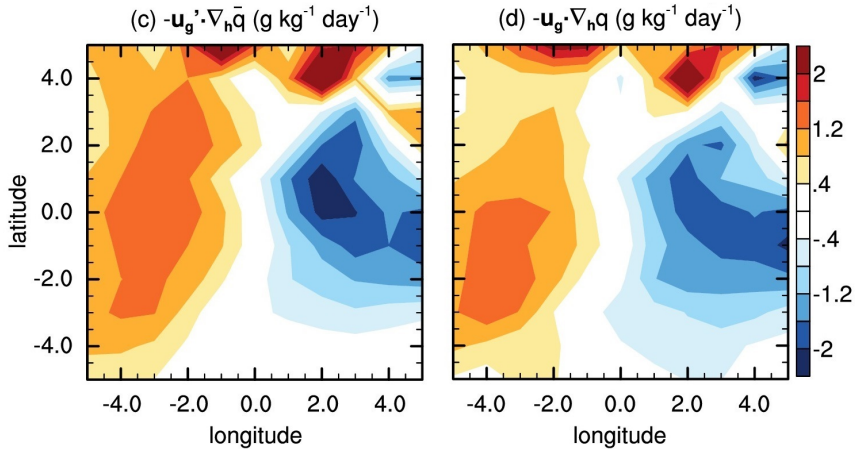


FIG. 8. Storm-centered composite mean longitude-height cross sections (upper panels) and 900 hPa map-view sections (lower panels) of the horizontal advection of specific humidity. The total field is depicted in the right panels, with the left panels depict the dominant term of the decomposition. Other minor terms are not plotted. Overbars and primes denote time-mean and anomalous quantities, respectively.

lower troposphere up-shear of the vortex. Diabatic heating also made a large contribution to the total QG ascent in the synoptic-scale events that caused the 2010 and 2014 floods in the foothills of the Himalayas (Shaevitz et al. 2016).

We now horizontally average the different components of QG ascent over the down-shear and up-shear regions depicted in Fig. 1. In the down-shear lower troposphere, the adiabatic ascent is sizable and even exceeds the diabatic ascent below 800 hPa (Fig. 7e). Above 500 hPa, diabatic QG ascent dominates, opposing the adiabatic subsidence at those levels. In the up-shear region, adiabatic QG descent exists throughout the free troposphere, with weak ascent confined below 850 hPa (Fig. 7f). Diabatic terms produce net QG ascent in the up-shear region, but of a weaker magnitude and a shallower vertical structure than in the down-shear region.

In both the down-shear and up-shear regions, the total QG vertical motion is roughly 70% of the total ascent estimated from YOTC (blue and black curves in Fig. 7e, f). This suggests that part of the vertical motion in MDs is not accounted for by QG dynamics, perhaps due to the omission of nonlinear terms associated with larger-Rossby number flow (the relative vorticity in Fig. 3b exceeds the planetary vorticity at the MD center, making the Rossby number greater than one there). Some ascent in MDs could also occur due to frictional ageostrophic flow; this has been hypothesized to be important in MDs (e.g., Goswami 1987), although friction seems to have an overall damping effect on MD intensity (Diaz and Boos 2019).

## vertical profiles of advection

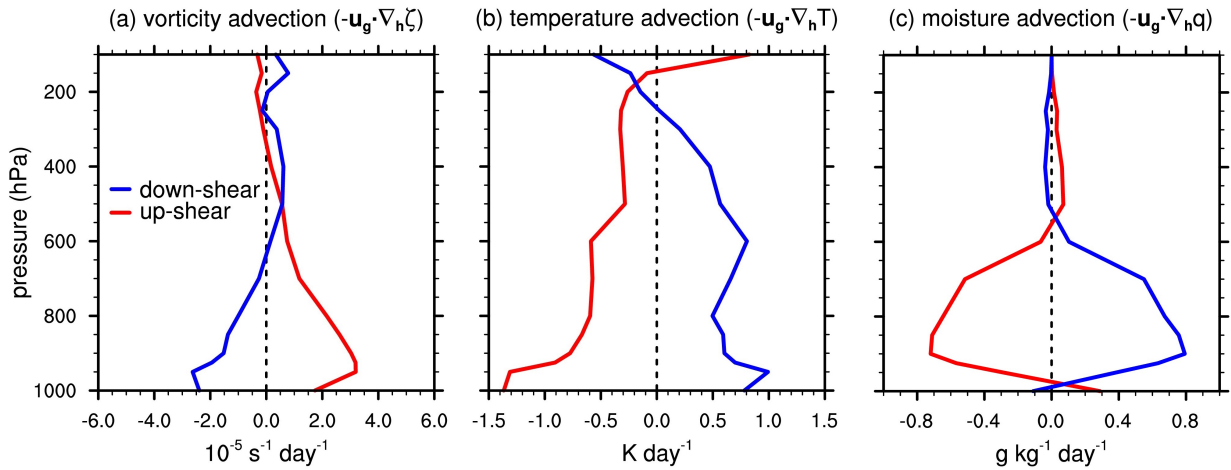


FIG. 9. Vertical profiles of horizontal advection of (a) absolute vorticity, (b) temperature, and (c) specific humidity in the regions down-shear (blue) and up-shear (red) of the MD center, respectively, from YOTC. The vertical profiles are obtained by horizontally averaging the computed variables in the black boxes depicted in Fig. 1.

### d. Horizontal moisture advection

Horizontal advection by cyclonic MD winds of a basic-state meridional moisture gradient formed the basis of the vortex-moisture instability mechanism proposed by Adames and Ming (2018a). In the YOTC storm-centered composite mean, horizontal moisture advection is structurally similar to horizontal temperature advection, with advection by the anomalous cyclonic winds of the poleward moisture gradient dominating (Fig. 8). This indeed results in moistening west of the vortex, where peak precipitating ascent is observed, and drying tendency to the east. The effect of these moisture tendencies on precipitating ascent is explored in section 4.

### 4. Results II: Idealized Modeling

Here we aim to understand the interaction between adiabatic and diabatic QG ascent, using the CQG modeling framework to couple a 3D CSRM with a 1D QG omega solver. The vertical profiles of vorticity and temperature advection required as inputs are obtained by horizontally averaging the storm-centered composite mean advective tendencies in the regions down-shear and up-shear of the MD center (black boxes in Fig. 1). Down-shear of center, vorticity advection increases with altitude in the lower and middle troposphere (Fig. 9a), while it decreases with altitude in the up-shear region. Temperature advection by cyclonic MD winds in the monsoonal poleward temperature gradient produces warming down-shear of the MD center and cooling up-shear (Fig. 9b). Horizontal moisture advection has a similar vertical structure, with moistening

and drying tendencies in the down-shear and up-shear regions, respectively (Fig. 9c).

The CQG framework requires choosing a characteristic horizontal wavelength,  $\lambda$  (see Eq. (2)). The horizontal distance along the direction of vertical shear that encompasses the positive and negative precipitation anomalies seems a suitable choice for  $\lambda$ , which we estimate to be roughly  $14^\circ$  or 1500 km. Alternatively, we obtain the 1D QG vertical velocity due to vorticity and temperature advection for various wavelengths, then choose the wavelength that provides QG vertical velocity closest to the values obtained from the 3D inversion in section 3. We perform 1D inversions with wavelengths of 500 km, 1000 km, and 1500 km using the vertical profiles of vorticity and temperature advection from the down-shear region (blue curves in Fig. 9). Ascent due to vorticity advection increases in magnitude with increasing wavelengths (Fig. 10a), while ascent due to temperature advection decreases in magnitude (Fig. 10b), consistent with Nie and Sobel (2016). The best match between the 1D and 3D results occurs for  $\lambda = 1500$  km, which we use in our integrations.

As described in section 2, all CSRM simulations are initialized from an RCE state with domain mean precipitation of about  $3.5 \text{ mm day}^{-1}$ . After several days, time-invariant horizontal moisture advection and adiabatic QG forcing in the form of temperature and vorticity advection are applied until day 20. A five-member ensemble is integrated for each model experiment, with each ensemble member varying by the day on which the adiabatic QG forcing and the horizontal moisture advection are switched on (between days 4 and 6, spaced at 12-hour intervals). All

### 1-D QG omega inversion: down-shear region

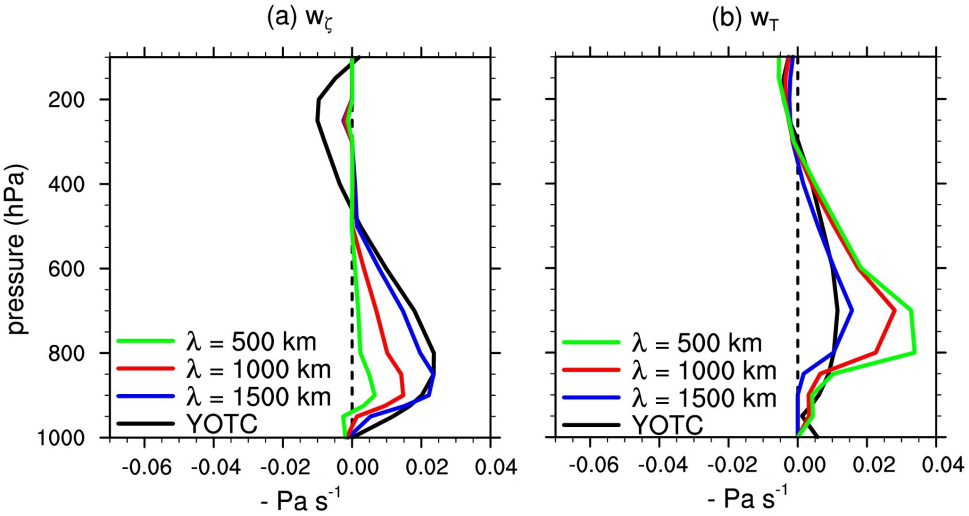


FIG. 10. Vertical profiles of QG ascent in the down-shear region due to (a) vorticity advection and (b) temperature advection obtained by inverting the 1D QG omega equation (i.e., Eq. (2)) for a range of characteristic wavelengths. The black curves in both panels are the respective vertical profiles obtained after horizontally averaging the results of the 3D inversion from YOTC in the region down-shear of the MD center.

time series are then shifted so that these forcings appear to be switched on at day 5. The change in precipitation due to the application of these forcings, compared to the RCE value, is our primary interest and quantifies the influence of the different processes on precipitation.

#### a. Down-shear precipitation

Precipitating ascent in the control experiment is influenced by QG adiabatic forcing, horizontal moisture advection, and surface enthalpy fluxes. In each ensemble member of the control, the domain mean precipitation increases over the 24 hours following the initial application of the forcings, peaking at about  $53 \text{ mm day}^{-1}$  then decreasing to fluctuate around  $39 \text{ mm day}^{-1}$  (thick black curve in Fig. 11). This represents a transient increase of  $50 \text{ mm day}^{-1}$  and a sustained increase of  $36 \text{ mm day}^{-1}$  compared to the RCE value. There is little scatter among the ensemble members, especially during the first 1-2 days following initiation of the forcings (one ensemble member was integrated to day 100, and the domain mean precipitation did not display any trends during this period).

The CQG framework may be most appropriate for assessing the transient response to a time-varying forcing, as discussed by Nie and Sobel (2016), since the QG omega equation is derived using formulations of the thermodynamic and vorticity equations in which the Eulerian time-tendency terms were retained. One can imagine an MD propagating into a particular geographic region in the monsoon basic state, and the associated adiabatic QG forcing transiently increasing precipitation to almost  $50 \text{ mm day}^{-1}$  over the course of a day in the air column at that

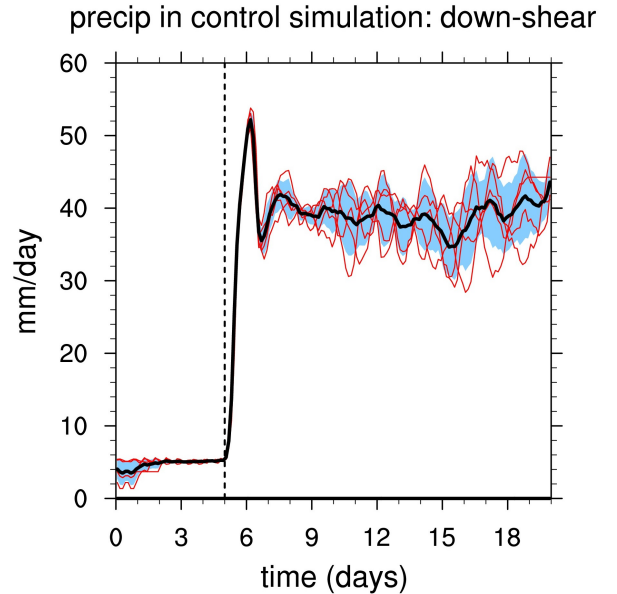


FIG. 11. Time series of domain mean precipitation in the ensemble of control simulations in the down-shear region. In this ensemble, the adiabatic QG forcing is switched on at various time steps between day 4 and 6. Precipitation in the individual ensemble members is depicted by thin red curves and the ensemble mean is represented by the thick black line. The light blue band shows one standard deviation across ensemble members relative to the ensemble mean. The vertical dashed black line denotes day 5, the average day across ensemble members when the adiabatic QG forcing is turned on. The precipitation is smoothed using a 6 hour running average.

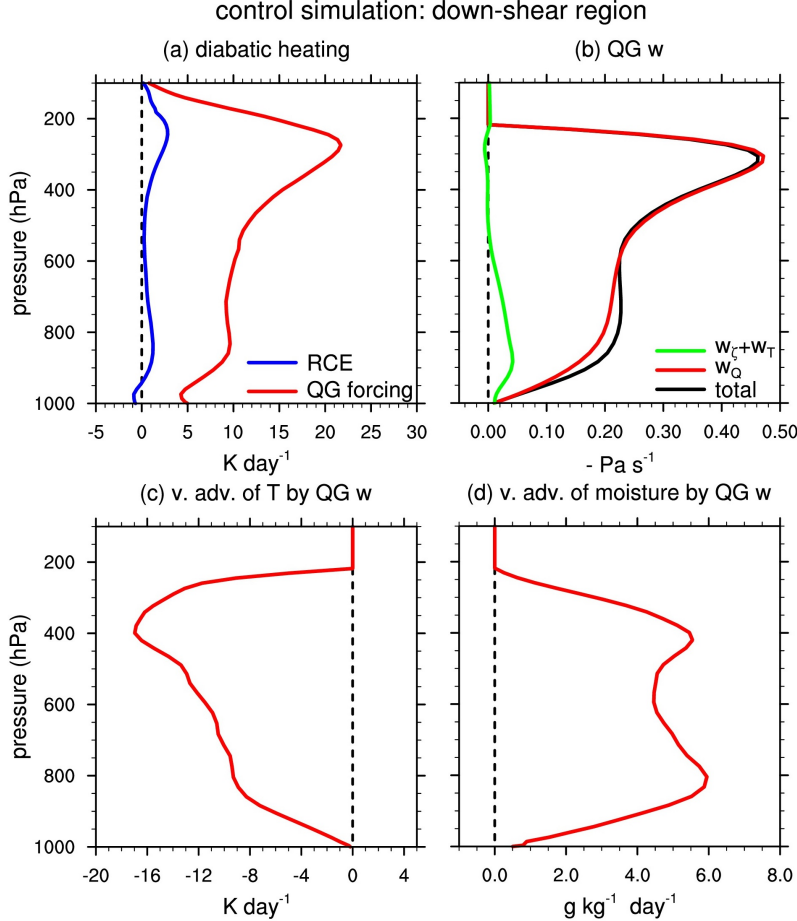


FIG. 12. Domain mean vertical profiles of (a) diabatic heating, (b) QG vertical velocity, (c) vertical temperature advection by QG vertical velocity, and (d) vertical advection of specific humidity by QG vertical velocity in the control simulation down-shear of the MD center in which the adiabatic QG forcing and horizontal moisture advection are applied on day 5. The red curves in all panels are temporally averaged between days 5 and 7. The blue curve in (a) corresponds to the RCE state and is temporally averaged between days 1 and 5.

location. At a typical MD propagation speed of  $2\text{-}3 \text{ m s}^{-1}$  (e.g. Boos et al. 2015), it would take about 3 days for an MD to travel roughly half of one wavelength  $\lambda$  and for its adiabatic QG forcing to thus cease acting on the precipitating phase of the disturbance. Furthermore, the background low-level westerlies and upper-level easterlies in the down-shear quadrant (Fig. 3a) would replace the air masses in the upper and lower troposphere on an even shorter time scale, eliminating any notion of the adiabatic QG forcing acting on a single Lagrangian air column for more than a day or so.

To mechanistically understand the influence of imposed adiabatic QG forcing on precipitating ascent, we examine vertical profiles of several variables in the control simulation. During the first 5 days, when the model is near RCE, the total diabatic heating from moist convection and radiation is roughly  $1 \text{ K day}^{-1}$  (blue curve in Fig. 12a). After adiabatic QG forcing is imposed, weak ascent of

peak magnitude near  $-5 \times 10^{-2} \text{ Pa s}^{-1}$  (green curve in Fig. 12b) vertically advects domain-mean temperature and moisture, cooling and moistening the lower troposphere. This makes the domain conducive to moist convection, increasing the diabatic heating, which results in stronger QG ascent, additional moistening and cooling by vertical advection, and more intense convection (Fig. 12b-d). The total QG ascent is strongly dominated by the diabatic QG ascent, with diabatic heating and vertical advective moistening contributing to a domain that is warmer and moister, respectively, than the initial RCE state (not shown).

The feedback of diabatic heating on QG ascent is central to the large enhancement of the precipitation rate, which we confirmed by conducting a separate simulation in which the diabatic term in the 1D QG omega equation was eliminated, making the total QG vertical motion purely adiabatic. In this simulation, the domain mean precipitation increased to only  $7 \text{ mm day}^{-1}$ , capturing less

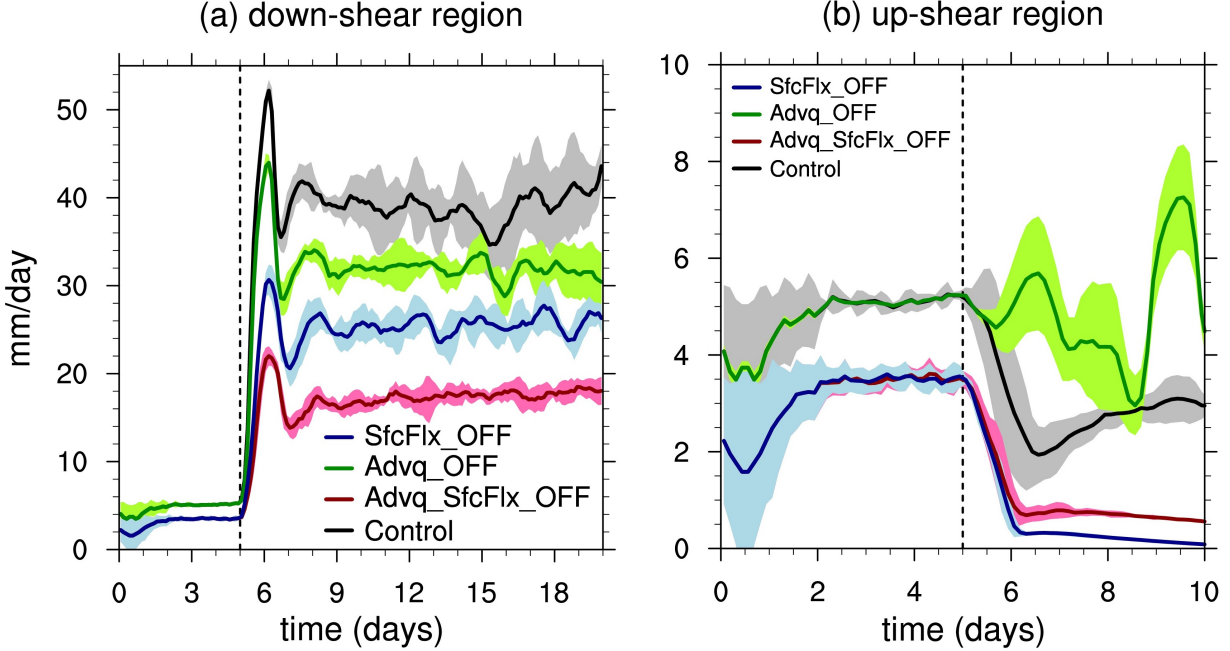


FIG. 13. Ensemble mean evolution of domain mean precipitation in the (a) down-shear and (b) up-shear regions simulations. The curves correspond to simulations in which the mean surface wind in the surface flux parameterization is set to zero (SfcFlx\_OFF, blue curve), moistening tendency due to the horizontal advection of moisture is switched off (Advg\_OFF, green curve), and both are switched off (Advg\_SfcFlx\_OFF, red curve). The black curve depicts the ensemble mean evolution of precipitation in the control simulation. The shaded band shows one standard deviation across ensemble members relative to the ensemble mean and the vertical dashed black line denotes day 5, the average day across ensemble members when the adiabatic QG forcing is turned on. Note the difference in axes scales between the two panels.

than 10% of the total increase of precipitation in the control simulation compared to RCE.

The diabatic QG vertical velocity obtained from our control CQE simulation is greater than the corresponding value in YOTC (e.g., compare red curves in Fig. 12b and Fig. 7e). This could potentially be due to the lack of explicit vertical wind shear in our CSRM, which can be detrimental to deep convection (wind shear appears implicitly in the adiabatic QG forcing, but its effect on individual convective updrafts, for example, is not represented). Additionally, the horizontal area of our CSRM domain (which is a  $128 \times 128$  km box) is considerably smaller than the area over which we average YOTC data (a  $5 \times 5^\circ$  box); nonlinearities in the diabatic feedback on QG ascent or in the sensitivity to horizontal moisture advection, for example, could result in the response to the area-averaged forcing being larger than the area-averaged response to the 3D forcing.

The final set of simulations pertaining to the down-shear region are designed to elucidate the relative importance of adiabatic QG forcing, horizontal moisture advection, and enhanced surface enthalpy fluxes. First, horizontal moisture advection is switched off and the background  $8 \text{ m s}^{-1}$  wind that was added to the wind speed used in the surface flux parameterization is eliminated (Advg\_SfcFlx\_OFF).

This greatly reduces the enhancement of precipitation that was seen in the control, with the domain-mean precipitation increasing to only  $22 \text{ mm day}^{-1}$  on day 6 (red curve in Fig. 13a). This increase, which is only due to the effect of adiabatic and diabatic QG ascent, accounts for roughly 40% of the total increase in precipitation in the control simulation. Next, when only horizontal moisture advection is switched off (Advg\_OFF, green curve in Fig. 13a), the domain mean precipitation peaks at  $44 \text{ mm day}^{-1}$ , indicating that horizontal moisture advection accounts for roughly 20% of the total increase in precipitation in the control simulation. Finally, when only the background surface wind is set to zero in the surface flux parameterization (SfcFlx\_OFF, blue curve in Fig. 13a), the maximum precipitation is  $30 \text{ mm day}^{-1}$ , showing that wind-enhanced surface enthalpy fluxes contribute roughly 40% of the increase in precipitation in the control simulation. The effect of wind-enhanced surface enthalpy fluxes is highly state-dependent, increasing precipitation by only  $2 \text{ mm day}^{-1}$  in the absence of adiabatic QG lifting, but by roughly  $20 \text{ mm day}^{-1}$  in the presence of QG ascent (compare red and green curves in Fig. 13a). These results are summarized in table 1.

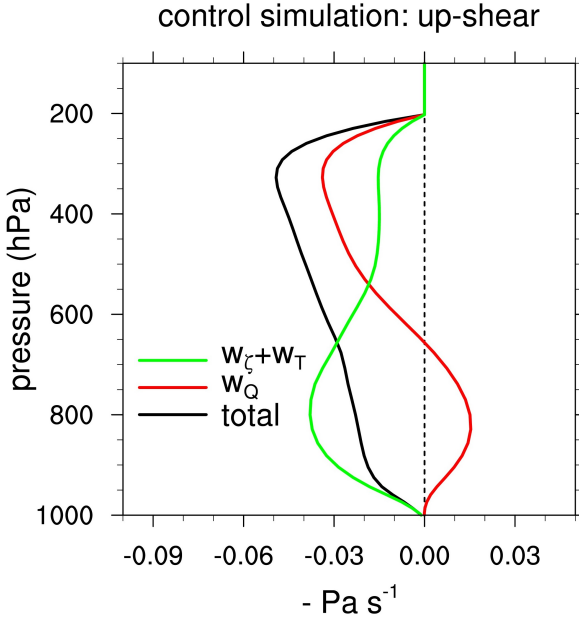


FIG. 14. Domain mean vertical profiles temporally averaged between days 6-10 of the QG vertical velocity in the control simulation up-shear of the MD center.

### b. Up-shear precipitation

The region up-shear of the MD center is characterized by adiabatic QG descent and drying by horizontal moisture advection, with both factors being unfavorable for deep convection. These effects will be opposed by the wind-enhancement of surface enthalpy fluxes, since the up-shear region still lies within the rotational flow of the MD. In the control CQE simulation of the up-shear region, the ensemble mean precipitation is roughly  $2 \text{ mm day}^{-1}$  on day 6, about  $1.5 \text{ mm day}^{-1}$  smaller than the RCE value (black curve in Fig. 13b). When the wind-enhanced surface enthalpy fluxes are removed from the control simulation, the ensemble mean precipitation drops even further to roughly  $0.3 \text{ mm day}^{-1}$  (SfcFlx\_OFF, blue curve in Fig. 13b), confirming that the wind-enhancement of surface enthalpy fluxes opposes the suppression of precipitation by adiabatic QG forcing and moisture advection in the up-shear region. When only the horizontal moisture advection is eliminated, the ensemble mean precipitation fluctuates considerably about a mean value of  $5.3 \text{ mm day}^{-1}$  (Advq\_OFF, green curve in Fig. 13b). Finally, when both horizontal moisture advection and enhanced surface fluxes are switched off, the ensemble mean precipitation is  $0.8 \text{ mm day}^{-1}$ , again considerably well below the RCE value (Advq\_SfcFlx\_OFF, red curve in Fig. 13b). In summary, these simulations indicate that wind-enhanced surface fluxes and horizontal advective drying each contribute about half the suppression of precipitation in the up-shear

TABLE 1. Difference between the transient domain mean precipitation measured on day 6 in all up-shear and down-shear simulations and the domain mean precipitation in RCE.

Process	Precipitation change	
	Down-shear	Up-shear
adiabatic QG lifting	3.5 mm/day (7%)	-2.5 mm/day
diabatic heating + adiabatic QG lifting	19 mm/day (39%)	-2.7 mm/day
horizontal moisture advection	8 mm/day (16%)	-0.5 to -3 mm/day
surface enthalpy flux	22 mm/day (45%)	2 to 4 mm/day
Total	49 mm/day (100%)	-1.5 mm/day

region, with adiabatic QG subsidence playing a relatively small role (table 1).

While the control simulation of the up-shear region has QG descent, the up-shear region in YOTC has weak QG ascent primarily due to diabatic heating (compare Fig. 14 with Fig. 7f). This difference could be due to the higher precipitation in the mean state of the region in which MDs form in the Bay of Bengal ( $16\text{-}20 \text{ mm day}^{-1}$ ) as compared to the RCE state used in our simulations ( $3.5 \text{ mm day}^{-1}$ ). These inconsistencies between YOTC and the CQG model in the up-shear region could also be due to differences between the 3D and 1D inversions of the QG omega equation used in YOTC and CQG, respectively. For example, the up-shear region in YOTC is characterized by adiabatic QG ascent below 800 hPa, whereas adiabatic QG descent occurs through the entire troposphere in the CQG model. The influence of our various forcings on precipitation in the up-shear region might change considerably if the basic state in the CQE model was more heavily precipitating.

## 5. Summary and Discussion

While theories for the intensification of MDs are an area of active research, the importance of moist convection in MD dynamics has long been recognized. The precipitating ascent that occurs down-shear, west and south-west of the MD center, has been attributed to adiabatic QG lifting and to horizontal moisture advection. Here we use an atmospheric reanalysis and idealized modeling to examine the influence of adiabatic QG forcing, horizontal moisture advection, and wind-enhanced surface enthalpy fluxes on precipitating ascent in MDs.

Storm-centered inversion of the 3D QG omega equation in the YOTC reanalysis shows that adiabatic QG lifting acts primarily in the lower troposphere of the down-shear quadrant, where adiabatic and diabatic QG ascent have comparable values. There is actually adiabatic QG subsidence in the upper troposphere of the downshear quadrant that opposes the much larger diabatic QG ascent there. This diagnostic analysis raises questions about how the adiabatic QG forcing influences moist convection in MDs

and how important it is compared to other processes such as horizontal moisture advection.

We use the CQG framework (Nie and Sobel 2016), to couple a 3D CSRM with a 1D QG omega equation solver. Vertical profiles of vorticity and temperature advection in regions down-shear and up-shear of the MD center, computed from YOTC reanalysis, are provided as inputs. These profiles of advection cause adiabatic QG ascent and descent down-shear and up-shear of the MD center, respectively. The adiabatic ascent, by vertically advecting moisture and temperature, makes the down-shear region more conducive to moist convection. In our idealized CQG framework, the feedback of moist convective heating on QG ascent accounts for roughly 40% of the increase in precipitation in the down-shear region compared to RCE. Wind-enhanced surface enthalpy fluxes also account for roughly 40%, and moistening by horizontal advection produces the remaining 20%. In the up-shear region, the temperature and vorticity advection produce adiabatic QG subsidence, but that subsidence has a small effect on precipitation. Drying by horizontal advection plays a larger role there, but its effects on precipitation are opposed by the influence of surface enthalpy fluxes that are enhanced by cyclonic winds in the MD.

The primary focus of this study has been the effect of QG forcing, horizontal moisture advection, and wind-enhanced surface enthalpy fluxes on moist convection down-shear of the MD center. This moist convection, and the associated diabatic heating, contribute to the intensification of the MD itself through stretching tendencies of absolute vorticity (or, alternatively, diabatic PV tendencies). Comparatively less attention has been provided to the region up-shear of the MD center, which is characterized by adiabatic QG descent and suppressed precipitation. A complete theory for the intensification of MDs would account for processes responsible for moist convection in the down-shear and up-shear regions as well as the contribution of deep convection to the intensification of the MD.

Finally, the idealized model used in this study has several important limitations. First, while vertical wind shear may play an important role in shaping moist convection in observed MDs, it enters our model only through the adiabatic QG forcing and is not explicitly present in our CSRM. This may alter the diabatic heating response to adiabatic QG lifting. Second, our framework does not include the effect of a progressively intensifying MD on adiabatic QG forcing and horizontal moisture advection, instead treating those processes as time-invariant. One might hope that there is a sufficiently large separation between the time scale of the convective response to adiabatic QG forcing and the time scale of MD intensification, but the former is about 1 day in our model while the latter has been observed to be 2-3 days (e.g. Sanders 1984; Diaz and Boos 2019). The CQG framework, in general,

does not allow the convective heating to feedback on the adiabatic QG forcing (Nie and Sobel 2016). A third limitation is that we used RCE as the basic state in our CSRM, while the mean state in which MDs form and intensify has strong precipitating ascent. However, much of the precipitation in that mean state is produced by the succession of monsoon lows and MDs that form over the Bay of Bengal each summer, so it may not be appropriate to impose the observed time-mean ascent in the basic state of the CSRM used in our framework. As with any problem in which the disturbances interact with the mean state, construction of an appropriate basic state based on observations can be a difficult task. Finally, our simulations used a prescribed radiative cooling and so do not include radiation-moisture interactions, which Adames and Ming (2018b) argued may be important for the intensification of MDs. Notwithstanding these caveats, the results of this study improve understanding of the factors influencing precipitating ascent in MDs, contributing to the eventual formation of a complete theory for the intensification of those storms.

**Acknowledgments.** This work was supported by Office of Naval Research award N00014-15-1-2531, by the U.S. Department of Energy, Office of Science, Biological and Environmental Research award DE-SC0019367, and by the Yale Center for Research Computing. We thank Ji Nie for providing the SAM-CQG modeling framework and for help with debugging issues. We thank Daniel Shaevitz for providing code to invert the 3D QG omega equation. ECMWF-YOTC data was accessed from the ECMWF Data Server, Reading, UK (<http://apps.ecmwf.int/datasets/data/yotc-od/>) in April 2017. The TRMM 3B42 gridded precipitation product was accessed from the NASA Goddard Earth Sciences Data and Information Services Center, Greenbelt, MD, USA ([https://disc.gsfc.nasa.gov/datasets/TRMM\\_3G25\\_V7](https://disc.gsfc.nasa.gov/datasets/TRMM_3G25_V7)) in May 2018.

## References

- Adames, Á. F., and Y. Ming, 2018a: Interactions between water vapor and potential vorticity in synoptic-scale monsoonal disturbances: Moisture vortex instability. *Journal of the Atmospheric Sciences*, **75** (6), 2083–2106, doi:10.1175/jas-d-17-0310.1, URL <https://doi.org/10.1175/jas-d-17-0310.1>.
- Adames, Á. F., and Y. Ming, 2018b: Moisture and moist static energy budgets of south asian monsoon low pressure systems in GFDL AM4.0. *Journal of the Atmospheric Sciences*, **75** (6), 2107–2123, doi:10.1175/jas-d-17-0309.1, URL <https://doi.org/10.1175/jas-d-17-0309.1>.
- Boos, W. R., J. V. Hurley, and V. S. Murthy, 2015: Adiabatic westward drift of indian monsoon depressions. *Quarterly Journal of the Royal Meteorological Society*, **141** (689), 1035–1048, doi:10.1002/qj.2454, URL <https://doi.org/10.1002/qj.2454>.

- Bretherton, C. S., M. E. Peters, and L. E. Back, 2004: Relationships between water vapor path and precipitation over the tropical oceans. *Journal of Climate*, **17** (7), 1517–1528, doi:10.1175/1520-0442(2004)017<1517:rbwvpa>2.0.co;2, URL [https://doi.org/10.1175/1520-0442\(2004\)017<1517:rbwvpa>2.0.co;2](https://doi.org/10.1175/1520-0442(2004)017<1517:rbwvpa>2.0.co;2).
- Cohen, N. Y., and W. R. Boos, 2016: Perspectives on moist baroclinic instability: Implications for the growth of monsoon depressions. *Journal of the Atmospheric Sciences*, **73** (4), 1767–1788, doi:10.1175/jas-d-15-0254.1, URL <https://doi.org/10.1175/jas-d-15-0254.1>.
- Davies, H. C., 2015: The quasigeostrophic omega equation: Reappraisal, refinements, and relevance. *Monthly Weather Review*, **143** (1), 3–25, doi:10.1175/mwr-d-14-00098.1, URL <https://doi.org/10.1175/mwr-d-14-00098.1>.
- Dee, D. P., and Coauthors, 2011: The ERA-interim reanalysis: configuration and performance of the data assimilation system. *Quarterly Journal of the Royal Meteorological Society*, **137** (656), 553–597, doi:10.1002/qj.828, URL <https://doi.org/10.1002/qj.828>.
- Diaz, M., and W. R. Boos, 2018: Barotropic growth of monsoon depressions. *Quarterly Journal of the Royal Meteorological Society*, doi:10.1002/qj.3467, URL <https://doi.org/10.1002/qj.3467>.
- Diaz, M., and W. R. Boos, 2019: Monsoon depression amplification by moist barotropic instability in a vertically sheared environment. *Quarterly Journal of the Royal Meteorological Society*, doi:10.1002/qj.3585, URL <https://doi.org/10.1002%2Fqj.3585>.
- Emanuel, K. A., 1986: An air-sea interaction theory for tropical cyclones. part i: Steady-state maintenance. *Journal of the Atmospheric Sciences*, **43** (6), 585–605, doi:10.1175/1520-0469(1986)043<0585:aasitf>2.0.co;2, URL [https://doi.org/10.1175/1520-0469\(1986\)043<0585:aasitf>2.0.co;2](https://doi.org/10.1175/1520-0469(1986)043<0585:aasitf>2.0.co;2).
- Fletcher, J. K., D. J. Parker, K. M. R. Hunt, G. Vishwanathan, and M. Govindankutty, 2018: The interaction of indian monsoon depressions with northwesterly midlevel dry intrusions. *Monthly Weather Review*, **146** (3), 679–693, doi:10.1175/mwr-d-17-0188.1, URL <https://doi.org/10.1175/mwr-d-17-0188.1>.
- Godbole, R. V., 1977: The composite structure of the monsoon depression. *Tellus*, **29** (1), 25–40, doi:10.3402/tellusa.v29i1.11327, URL <https://doi.org/10.3402/tellusa.v29i1.11327>.
- Goswami, B. N., 1987: A mechanism for the west-north-west movement of monsoon depressions. *Nature*, **326** (6111), 376–378, doi:10.1038/326376a0, URL <https://doi.org/10.1038/326376a0>.
- Holton, J. R., and G. J. Hakim, 2013: Introduction. *An Introduction to Dynamic Meteorology*, Elsevier, 1–29, doi:10.1016/b978-0-12-384866-6.00001-5, URL <https://doi.org/10.1016/b978-0-12-384866-6.00001-5>.
- Houze, R. A., 1997: Stratiform precipitation in regions of convection: A meteorological paradox? *Bulletin of the American Meteorological Society*, **78** (10), 2179–2196, doi:10.1175/1520-0477(1997)078<2179:spiroc>2.0.co;2, URL [https://doi.org/10.1175/1520-0477\(1997\)078<2179:spiroc>2.0.co;2](https://doi.org/10.1175/1520-0477(1997)078<2179:spiroc>2.0.co;2).
- Hunt, K. M. R., A. G. Turner, P. M. Inness, D. E. Parker, and R. C. Levine, 2016: On the structure and dynamics of indian monsoon depressions. *Monthly Weather Review*, **144** (9), 3391–3416, doi:10.1175/mwr-d-15-0138.1, URL <https://doi.org/10.1175/mwr-d-15-0138.1>.
- Hurley, J. V., and W. R. Boos, 2015: A global climatology of monsoon low-pressure systems. *Quarterly Journal of the Royal Meteorological Society*, **141** (689), 1049–1064, doi:10.1002/qj.2447, URL <http://dx.doi.org/10.1002/qj.2447>.
- Khairoutdinov, M. F., and D. A. Randall, 2003: Cloud resolving modeling of the ARM summer 1997 IOP: Model formulation, results, uncertainties, and sensitivities. *J. Atmos. Sci.*, **60** (4), 607–625, doi:10.1175/1520-0469(2003)060<0607:crmota>2.0.co;2, URL [http://dx.doi.org/10.1175/1520-0469\(2003\)060<0607:CRMOTA>2.0.CO;2](http://dx.doi.org/10.1175/1520-0469(2003)060<0607:CRMOTA>2.0.CO;2).
- Krishnamurti, T. N., M. Kanamitsu, R. Godbole, C.-B. Chang, F. Carr, and J. H. Chow, 1976: Study of a monsoon depression (II), dynamical structure. *Journal of the Meteorological Society of Japan. Ser. II*, **54** (4), 208–225, doi:10.2151/jmsj1965.54.4.208, URL <https://doi.org/10.2151/jmsj1965.54.4.208>.
- Lindzen, R. S., B. Farrell, and A. J. Rosenthal, 1983: Absolute barotropic instability and monsoon depressions. *Journal of the Atmospheric Sciences*, **40** (5), 1178–1184, doi:10.1175/1520-0469(1983)040<1178:abiamd>2.0.co;2, URL [https://doi.org/10.1175/1520-0469\(1983\)040<1178:abiamd>2.0.co;2](https://doi.org/10.1175/1520-0469(1983)040<1178:abiamd>2.0.co;2).
- Moncrieff, M. W., D. E. Waliser, M. J. Miller, M. A. Shapiro, G. R. Asrar, and J. Caughey, 2012: Multiscale convective organization and the YOTC virtual global field campaign. *Bulletin of the American Meteorological Society*, **93** (8), 1171–1187, doi:10.1175/bams-d-11-00233.1, URL <https://doi.org/10.1175/bams-d-11-00233.1>.
- Montgomery, M. T., J. Persing, and R. K. Smith, 2015: Putting to rest WISHE-ful misconceptions for tropical cyclone intensification. *J. Adv. Model. Earth Syst.*, **7** (1), 92–109, doi:10.1002/2014ms000362, URL <http://dx.doi.org/10.1002/2014ms000362>.
- Montgomery, M. T., N. V. Sang, R. K. Smith, and J. Persing, 2009: Do tropical cyclones intensify by WISHE? *Quarterly Journal of the Royal Meteorological Society*, **135** (644), 1697–1714, doi:10.1002/qj.459, URL <http://dx.doi.org/10.1002/qj.459>.
- Moorthi, S., and A. Arakawa, 1985: Baroclinic instability with cumulus heating. *Journal of the Atmospheric Sciences*, **42** (19), 2007–2031, doi:10.1175/1520-0469(1985)042<2007:biwch>2.0.co;2, URL [https://doi.org/10.1175/1520-0469\(1985\)042<2007:biwch>2.0.co;2](https://doi.org/10.1175/1520-0469(1985)042<2007:biwch>2.0.co;2).
- Murthy, V. S., and W. R. Boos, 2018: Role of surface enthalpy fluxes in idealized simulations of tropical depression spinup. *Journal of the Atmospheric Sciences*, **75** (6), 1811–1831, doi:10.1175/jas-d-17-0119.1, URL <https://doi.org/10.1175/jas-d-17-0119.1>.
- Nie, J., D. A. Shaevitz, and A. H. Sobel, 2016: Forcings and feedbacks on convection in the 2010 pakistan flood: Modeling extreme precipitation with interactive large-scale ascent. *Journal of Advances in Modeling Earth Systems*, **8** (3), 1055–1072, doi:10.1002/2016ms000663, URL <https://doi.org/10.1002/2016ms000663>.
- Nie, J., and A. H. Sobel, 2016: Modeling the interaction between quasi-geostrophic vertical motion and convection in a single column. *Journal of the Atmospheric Sciences*, **73** (3), 1101–1117, doi:10.1175/jas-d-15-0205.1, URL <https://doi.org/10.1175/jas-d-15-0205.1>.
- Ramage, C. S., 1971: *Monsoon Meteorology*. Elsevier, doi:10.1016/s0074-6142(08)x6034-6, URL [https://doi.org/10.1016/s0074-6142\(08\)x6034-6](https://doi.org/10.1016/s0074-6142(08)x6034-6).
- Raymond, D. J., and H. Jiang, 1990: A theory for long-lived mesoscale convective systems. *Journal of the Atmospheric Sciences*, **47** (24), 3067–3077, doi:10.1175/1520-0469(1990)047<3067:atflm>2.0.co;

- 2, URL [https://doi.org/10.1175/1520-0469\(1990\)047<3067:atflm>2.0.co;2](https://doi.org/10.1175/1520-0469(1990)047<3067:atflm>2.0.co;2).
- Saha, K., and C.-P. Chang, 1983: The baroclinic processes of monsoon depressions. *Monthly Weather Review*, **111** (7), 1506–1514, doi:10.1175/1520-0493(1983)111<1506:tbpmnd>2.0.co;2, URL [https://doi.org/10.1175/1520-0493\(1983\)111<1506:tbpmnd>2.0.co;2](https://doi.org/10.1175/1520-0493(1983)111<1506:tbpmnd>2.0.co;2).
- Sanders, F., 1984: Quasi-geostrophic diagnosis of the monsoon depression of 5–8 July 1979. *Journal of the Atmospheric Sciences*, **41** (4), 538–552, doi:10.1175/1520-0469(1984)041<0538:qgdotm>2.0.co;2, URL [https://doi.org/10.1175/1520-0469\(1984\)041<0538:qgdotm>2.0.co;2](https://doi.org/10.1175/1520-0469(1984)041<0538:qgdotm>2.0.co;2).
- Shaevitz, D. A., J. Nie, and A. H. Sobel, 2016: The 2010 and 2014 floods in India and Pakistan: dynamical influences on vertical motion and precipitation. *ArXiv e-prints*, 1603.01317.
- Sikka, D. R., 1977: Some aspects of the life history, structure and movement of monsoon depressions. *Pure and Applied Geophysics PAGEOPH*, **115** (5–6), 1501–1529, doi:10.1007/bf00874421, URL <https://doi.org/10.1007/bf00874421>.
- Yoon, J.-H., and T.-C. Chen, 2005: Water vapor budget of the Indian monsoon depression. *Tellus A*, **57** (5), 770–782, doi:10.1111/j.1600-0870.2005.00145.x, URL <https://doi.org/10.1111/j.1600-0870.2005.00145.x>.